Journal of Materials Chemistry A

PAPER

View Article Online
View Journal | View Issue

Cite this: J. Mater. Chem. A, 2014, 2, 6549

Combination of a SnO_2–C hybrid anode and a tubular mesoporous carbon cathode in a high energy density non-aqueous lithium ion capacitor: preparation and characterisation†

Wen-Hui Qu, Fei Han, An-Hui Lu, Chao Xing, Mo Qiao and Wen-Cui Li*

Received 8th February 2014
Accepted 17th February 2014

DOI: 10.1039/c4ta00670d

www.rsc.org/MaterialsA

Lithium ion capacitors (LICs), bridging supercapacitors and lithium ion batteries (LIBs), have recently drawn considerable attention. In this report, a non-aqueous LIC was fabricated using tubular mesoporous carbon as a cathode and a SnO_2–C hybrid (ultrafine SnO_2 encapsulated in the tubular mesoporous carbon) as an anode. Such a LIC can achieve a maximum energy density of 110 W h kg^{-1} and a maximum power density of 2960 W kg^{-1}. The capacitance retention is fairly stable and retains 80% of its initial value after 2000 cycles. This unique performance arises because of the highly conductive tubular mesoporous carbon matrix and fast charge/ion diffusion in the SnO_2–C hybrid anode. It is shown that the SnO_2 loading in the anode has a great influence on the stability of the SnO_2 nano-structure and the kinetics of lithium ion transfer. Electrochemical impedance spectroscopy (EIS) was used to evaluate the charge transfer resistance and the ionic diffusion resistance before and after long-term cycling. The diffusion coefficient was also calculated to verify the good rate and cycling capability.

1. Introduction

The development of energy storage devices such as lithium ion batteries (LIBs) and supercapacitors is being actively promoted in order to improve energy utilization efficiency.[1] Although a supercapacitor is effective for instantaneous charge–discharge of large current supplies, it is limited by low energy densities.[2] It exhibits a high specific power compared with other rechargeable electrochemical energy storage devices, typically above 10 kW kg^{-1}, and a low specific energy density, typically below 10 W h kg^{-1}. On the other hand, LIBs have the advantage of high energy densities (150–200 W h kg^{-1}), but deliver relatively low power densities compared with supercapacitors.[3,4] Moreover, LIBs suffer from a limited cycle-life (usually 500–1000 cycles) and lack the ability to safely allow fast charging due to Li metal deposition. Therefore, there is a need to fill a critical void in the power/energy spectrum by designing new and/or improved devices and to improve the long-term cycling performance of the devices.

The lithium ion capacitor (LIC), a supercapacitor–battery hybrid energy storage system, can not only overcome the energy density limitation of conventional supercapacitors but also improve the power output of lithium ion batteries.[5–7] The LIC system usually combines one electrode which is charged by a redox reaction with the other electrode where the charge is stored in an electrochemical double layer. To widen the potential window and further increase the energy density, a non-aqueous LIC has been developed integrating lithium ion intercalation compounds with porous carbon.[8–15]

Lithium ion intercalation compounds for LICs have been investigated in the past, such as hard carbon,[13] graphite,[9,11] graphene[15,16] and, in particular, $Li_4Ti_5O_{12}$.[8,10,12] In 2001, an anode of the $Li_4Ti_5O_{12}$ intercalation compound and a cathode of porous carbon were incorporated into a non-aqueous LIC cell.[8] $Li_4Ti_5O_{12}$ commonly exhibits a high surface stability and has a long cycle life, whereas its high voltage plateau and low theoretical capacity (175 mA h g^{-1}) limit its energy/power performance.[17–19] Although graphite is a standard anode active material in both lithium-ion battery research and commercial products, lithium plating and re-intercalation of the plated lithium into the graphite both occur because of the low voltage of Li^+ intercalation (close to −3 V *vs.* SHE).[20] This results in a low charging capacity during fast charge protocols. Metal oxides can offer a high theoretical capacity (*i.e.* 782 mA h g^{-1} for SnO_2, 924 mA h g^{-1} for Fe_3O_4, and 890 mA h g^{-1} for Co_3O_4)[21–26] and relatively low intercalation potential, which is extremely promising for their application in LICs. However, they still suffer poor capacity retention and unsatisfactory rate performance due to their severe pulverization and slow kinetics of charge/ion diffusion in these materials.[27] Thus, carbon-coating was used to improve the lithiation rate capability.[28–30]

State Key Laboratory of Fine Chemicals, School of Chemical Engineering, Dalian University of Technology, Dalian 116024, P. R. China. E-mail: wencuili@dlut.edu.cn; Fax: +86-411-84986355

† Electronic supplementary information (ESI) available. See DOI: 10.1039/c4ta00670d

Recently, we have reported a SnO_2–C hybrid fabricated by encapsulating nanosized SnO_2 particles into TMC for a LIB anode. The tubular hybrid exhibits not only a considerably high reversible capacity, up to 1039 mA h g^{-1} after 100 cycles, but also fast charge–discharge kinetics at a high current density.[31] It is well known that the electrochemical performance is highly dependent on the intrinsic crystalline texture and structure of the active materials. The excellent performance of the SnO_2–C hybrid is ascribed to the following structural characteristics: (I) fast charge transfer and small ionic diffusion length in SnO_2 nanoparticles (4–5 nm); (II) a high surface area SnO_2–C hybrid for a more active interface; (III) efficient contact between active particles and carbon walls; (IV) open pore channels and a large pore volume for hosting a high amount of SnO_2 and allowing volume expansion during Li^+ insertion/extraction.

Motivated by these structural features and superior electrochemical performance in LIB anodes, we developed a non-aqueous LIC based on the SnO_2–C hybrid as an anode. Three porous carbons were used as the LIC cathode. These were the home-made TMC, hierarchical porous carbon (HPC) and a commercial microporous carbon YP47. Among them, TMC exhibits the highest capacitance and good rate capability. We therefore used the TMC as the cathode, adjusted the SnO_2 content in the anode and assembled a LIC with the two electrodes. The obtained LIC shows a maximum energy density of 110 W h kg^{-1} (at a power density of 173 W kg^{-1}) and a maximum power density of 2960 W kg^{-1}. After 2000 charge–discharge cycles, the achieved capacitance retains 80% of its original value at a current density of 1 A g^{-1}, which is higher than that of previous LICs based on a metal oxide anode.[32–34] To further explore the interaction between the SnO_2 nanoparticles and the carbon matrix, we established a correlation between the ionic diffusion rate and the SnO_2 loading ratio in the anode using EIS. It is interesting to note that an optimum loading ratio leads to the highest ionic diffusion speed after many cycles.

2. Experimental

2.1 Materials synthesis

Porous carbon cathode. The TMC with a two-dimensional hexagonal array of tubes was synthesized by a nanocasting process using SBA-15 as a template, furfuryl alcohol as the carbon source and oxalic acid as a catalyst.[35–37] HPC was prepared by the direct pyrolysis of a copolymer of resorcinol with formaldehyde, and subsequently by physical activation with CO_2.[38] YP47 is a commercial microporous carbon (Kuraray, Japan). The TEM images of TMC and HPC are shown in Fig. S1.†

SnO_2–C hybrid. The SnO_2–C hybrid was synthesized by a repeated impregnation–conversion step as follows:[31] (I) impregnation step: 300 mg $SnCl_4 \cdot 5H_2O$ (99%) as the tin precursor was dissolved in 300 μL of deionized water. The $SnCl_4$ aqueous solution was added to 0.1 g porous carbon under stirring at 25 °C. (II) Conversion step: after all the solutions had been absorbed, the powder was put into a Teflon bottle where a small container containing 4 mL ammonia solution (14%) was placed in advance, that ensured no direct contact between the powder and the ammonia solution. After sealing, the bottle was heated at 90 °C for 3 h. The product was then washed several times with deionized water and ethanol, and dried at 90 °C. The impregnation and conversion steps were repeated several times in order to increase the SnO_2 content. Finally, the hybrid was heated to 300 °C and kept at this temperature for 1 h, and 550 °C for 3 h in an argon atmosphere. The SnO_2 loadings of three SnO_2–C hybrids were measured to be 40%, 57% and 75% by thermogravimetric analysis (TGA). The samples were named SnO_2(40)–C, SnO_2(57)–C and SnO_2(75)–C.

2.2 Materials characterization

Transmission electron microscopy (TEM) analysis was carried out with a FEI Technai F30 instrument operating at 200 kV. Some TEM images were also obtained using a Hitachi HF2000 transmission electron microscope equipped with a cold field emission gun. For TEM observation of the dispersion and sizes of the SnO_2 nanoparticles, samples were embedded in Spur's resin and cut into 60 nm thin sections using a microtome. Nitrogen adsorption isotherms were measured at 77.4 K with a Tristar 3000 sorption analyzer (Micromeritics Instruments, USA). The Brunauer–Emmett–Teller (BET) method was used to calculate the specific surface area (S_{BET}). Pore size distributions (PSDs) were calculated from the adsorption branches of the isotherms using the Barrett–Joyner–Halenda (BJH) model for mesopores. Total pore volumes (V_{total}) were determined from the amount adsorbed at a relative pressure, P/P_0, of 0.99. Micropore volumes (V_{micro}) were calculated using the *t*-plot method. X-ray diffraction (XRD) patterns of the samples were recorded with a Rigaku D/Max 2400 diffractometer in the Bragg Brentano (reflection) geometry using Cu Kα radiation (40 kV, 100 mA, $\lambda = 1.5406$ A). TGA was performed in air from room temperature to 800 °C with a heating rate of 10 °C min^{-1} on an STA449 F3 Jupiter thermogravimetric analyzer (NETZSCH).

2.3 Electrochemical characterization

The anode was prepared by mixing SnO_2–C with polyvinylidene fluoride (PVDF, DuPont, USA) and a conductive carbon black additive (Super P, TIMCAL Switzerland) (8 : 1 : 1 in mass) in *N*-methyl-2-pyrrolidone (NMP). Cu foil with a surface area of 1.13 cm^2 was used as the current collector. The mass of the active material was approximately 1–2 mg and two electrodes with identical weights were selected for the measurements. The cathode was fabricated by mixing the porous carbon sample with 10 wt% carbon black and 10 wt% PVDF binder. The mixture (4–8 mg) was pressed onto an Al foil current collector.

All cells were fabricated in an argon-filled glove box. The porous carbon cathode and SnO_2–C anode materials were first tested in a half cell designed with the Li metal as the counter and reference electrodes. Two-electrode LIC cells were assembled in a liquid electrolyte consisting of 1 M $LiPF_6$ in a dimethyl carbonate (DMC), ethyl methyl carbonate (EMC) and ethylene carbonate (EC) (1 : 1 : 1 v/v/v) solution. Before assembly, the SnO_2–C electrode was prelithiated by placing the electrolyte-wetted electrode in full contact with the Li metal for 60 min. The mass ratio of the cathode–anode active material was 3.9 : 1. The electrodes were separated by a Celgard 2400 battery membrane

soaked in the electrolyte. The open-circuit voltage (OCV) of both the three-electrode and two-electrode cells was about 2.6–2.9 V.

The charge–discharge measurements of a SnO_2–C half cell were carried out at different current densities on a Land CT2001A battery test system. The specific capacity of the SnO_2–C hybrids was calculated based on the total mass of SnO_2 and carbon. Cyclic voltammetry (CV), galvanostatic charge–discharge cycling (GC) and electrochemical impedance spectroscopy (EIS) for all cells were performed on a CHI660D electrochemical workstation (CH Instruments, China) at room temperature. Stability measurements of the LIC were carried out using an Arbin BT2000 multi-channel college station (Arbin Instruments, USA). The specific capacitance (C) of the single electrode was calculated from the discharge curve based on the following formula:

$$C = \frac{I\Delta t}{\Delta V} \quad (1)$$

where I (A g^{-1}) is the discharge current based on the mass of the active material, Δt (s) is the discharge time, and ΔV (V) is the potential window from the end of the internal resistance (R) drop to the end of the discharge process.

The specific capacitance of a LIC cell (C_{cell}) was calculated from the discharge process after 20 cycles' activation, according to the formula below:

$$C_{cell} = \frac{I\Delta t}{\Delta V} \quad (2)$$

where I (A g^{-1}) is the discharge current based on the total mass of the active material in the anode and cathode, the definitions of Δt (s) and ΔV (V) are as the same as those in formula (1). The energy density (E) was obtained from the capacitance of the LIC cells:

$$E = \frac{C_{cell}V^2}{2 \times 3.6} \quad (3)$$

The power density (P) of a LIC was determined by:

$$P = \frac{3600 \times E}{\Delta T} \quad (4)$$

where Δt (s) is the discharge time.

3. Results and discussion

3.1 Cathode properties

As cathodes of LICs, porous carbons are required to possess an exceptional capacitance and an extremely fast charge–discharge rate performance. Porous carbons with high surface areas have an exceptional propensity for anion double-layer adsorption as demonstrated in non-aqueous EDLCs.[39,40] The capacitive adsorption process can fulfill the requirements at 1.0–4.5 V *vs.* Li/Li^+ in a $LiPF_6$-containing organic electrolyte.[41]

The three kinds of porous carbon chosen as the cathode (TMC, HPC and YP47) were characterized by using the nitrogen adsorption technique. Fig. 1a and b show nitrogen sorption isotherms and corresponding PSDs of all three porous carbons. The calculated structure parameters are listed in Table 1. YP47 is

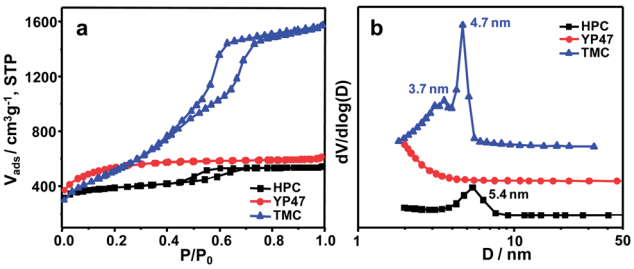

Fig. 1 (a) N_2 sorption isotherms and (b) pore size distributions (PSDs) of HPC, YP47 and TMC.

Table 1 Structural parameters of the porous carbons

Sample	S_{BET}/m^2 g^{-1}	V_{total}/cm^3 g^{-1}	V_{micro}/cm^3 g^{-1}	D_{peak}/nm	C_g[a]/F g^{-1}
HPC	1323	0.84	0.42	5.4	64
YP47	1869	0.94	0.84	—	84
TMC	1852	2.4	0.12	4.7 & 3.6	120

[a] The gravimetric capacitance was calculated from GC curves at a current density of 0.5 A g^{-1} in a Li anode half-cell system.

a commercial microporous carbon that possesses a high surface area and abundant microporosity. The nitrogen sorption isotherms of TMC and HPC (Fig. 1a) are essentially of type IV with a pronounced hysteresis loop, indicating mesoporous characteristics. TMC exhibits a higher BET surface area and larger pore volume compared with HPC due to its unique structure, *i.e.* the tubular structure that provides a "double" surface and more void space. The as-synthesized HPC is a hierarchical micro- and mesoporous carbon, in which the micropores and smaller mesopores are the major contributors to the pore volume.

To evaluate the electrochemical performance of the porous carbons, their cathode half cells were fabricated with a Li foil as the anode. The potential window is between 2 and 4.5 V *vs.* Li/Li^+. As the cell is charged, Li^+ is reduced at the Li metal anode and the PF_6^- anion is adsorbed onto double layers on the cathode. Cyclic voltammetry was carried out to determine the capacitive behavior of the porous carbons. The representative CV behavior of HPC, YP47 and TMC is shown in Fig. 2a. Relatively flat rectangular-shaped profiles are evident at a scan rate of 5 mV s^{-1} and no Faradaic reactions are observed. Galvanostatic charge–discharge curves shown in Fig. 2b were used to calculate the gravimetric capacitance. They are triangular in shape and exhibit only small ohmic drops at high currents related to the resistivity of the half-cells. The capacitance of the porous carbons as a function of current density is shown in Fig. 2c. The capacitance of TMC at 0.3 A g^{-1} is 127 F g^{-1}, almost twice that of HPC and is 83 F g^{-1} at 2 A g^{-1}.

TMC has a large capacitance and good rate capability because of the high surface area (>1500 m^2 g^{-1}) and open porosity. Fig. 2d shows a representative plot of the capacitance of TMC. As expected for the capacitive adsorption process, the voltage increases linearly with capacitance. Based on the excellent electrochemical properties, TMC was chosen as the cathode material for the subsequently fabricated lithium ion capacitor.

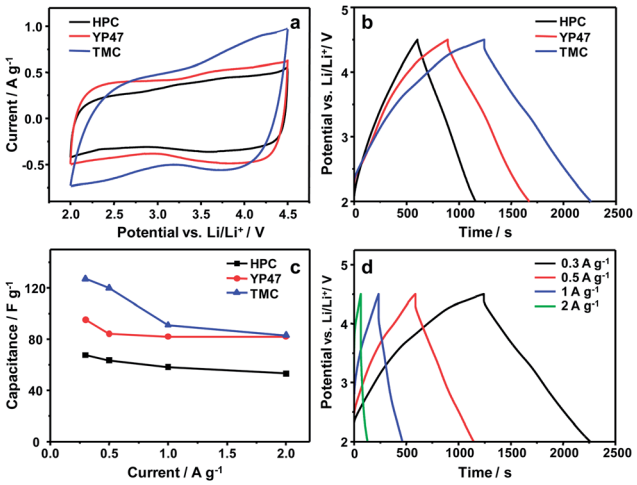

Fig. 2 (a) CV curves of HPC, YP-47 and TMC at a scan rate of 5 mV s^{-1}, (b) galvanostatic charge–discharge curves of HPC, YP-47 and TMC at a current density of 0.3 A g^{-1}, (c) capacitances of HPC, YP-47 and TMC with increasing current density, and (d) GC curves of TMC at different current densities.

3.2 Anode properties

The SnO_2 content in the hybrid was controlled by repeating the impregnation and ammonia treatment. A detailed synthesis method of the SnO_2–C hybrid is included in the Experimental section. The TMC mentioned above was chosen as a carbon matrix because it has a large pore volume offering possibility for high SnO_2 loading, thus potentially high specific capacity. As shown in Fig. 3a, TGA of SnO_2–C in air reveals that the weight fractions of SnO_2 in the hybrids are 40 wt%, 57 wt% and 75 wt%. The content was calculated based on the mass loss below 600 °C which was attributed to the combustion of carbon. Such a high content of nanocrystalline SnO_2, in association with TMC as the matrix that has tubular mesopore channels, thin carbon walls, a high pore volume and abundant conducting pathways, results in a high capacity and excellent cycling performance when they are used for lithium storage.[42,43]

XRD patterns in Fig. 3b can be assigned to extremely fine nanocrystalline SnO_2 without other phases detected in the samples. The peaks correspond to the (110), (101), (200) and (211) crystal planes of cassiterite (JCPDF#41-1445).[44] The crystallite size is estimated to be in the range of 3–6 nm from the Scherrer equation.[45,46] The formation of such nanocrystalline SnO_2 results from the confinement effect of the tubular walls in the TMC matrix.

The pore parameters of the SnO_2–C hybrids were examined by nitrogen sorption at 77.4 K. As can be seen in Fig. 3c, the nitrogen sorption isotherms of samples SnO_2(40)–C and SnO_2(57)–C are both of type IV with hysteresis loops in the relative pressure (P/P_0) range of 0.40–0.65, reflecting the mesoporous characteristics. The BET surface area and pore volume

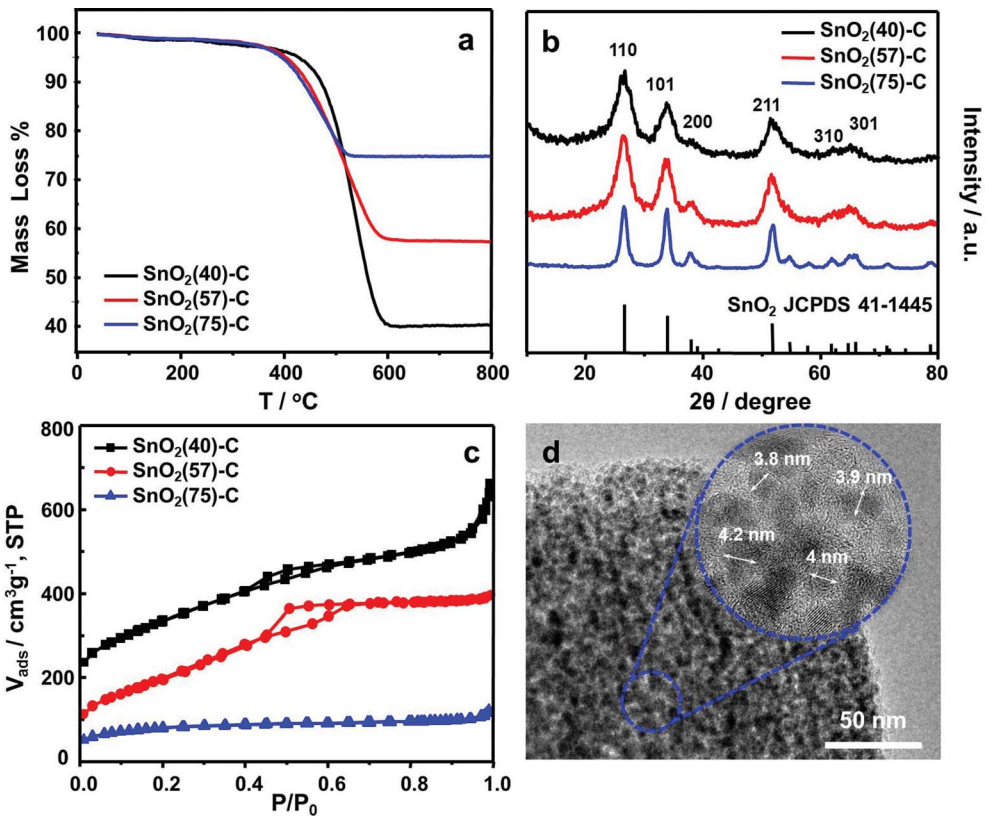

Fig. 3 (a) TG curves of SnO_2(40)–C, SnO_2(57)–C and SnO_2(75)–C, (b) wide-angle XRD patterns, (c) N_2 sorption isotherms of SnO_2(40)–C, SnO_2(57)–C and SnO_2(75)–C (the SnO_2(40)–C isotherm is offset vertically by 100 cm^3 g^{-1}), and (d) TEM image of SnO_2(57)–C. The inset is a magnified view of the SnO_2(57)–C hybrid.

are quite large at 726 $m^2 g^{-1}$ and 0.62 $cm^3 g^{-1}$ for SnO_2(57)–C and 856 $m^2 g^{-1}$ and 0.87 $cm^3 g^{-1}$ for SnO_2(40)–C, respectively. Such a large surface area may offer a sufficient interface to facilitate the electrochemical reactions. The PSDs (see Fig. S2†) of the two materials calculated by the BJH method show a bimodal pore system, proving that the pore structure of the carbon support is well-preserved after immobilization of SnO_2 nanoparticles. However, a type I nitrogen sorption isotherm of SnO_2(75)–C is observed without hysteresis loops, indicating microporous characteristics with a BET surface area of 283 $m^2 g^{-1}$ and a pore volume of 0.19 $cm^3 g^{-1}$. The disappearance of the mesoporous structure is attributed to the high loading ratio of SnO_2 into the pore system.

Fig. 3d shows a TEM image of the SnO_2–C hybrid with a 57 wt% SnO_2 loading. Although the image of only one sample is shown, the structure and particle size distribution of all samples are very similar. The well dispersed SnO_2 nanoparticles with a uniform size are homogeneously encapsulated in the mesoporous channels of TMC. No obvious SnO_2 agglomerations are observed on the external surface of SnO_2–C and the structure of the carbon matrix is well preserved, implying the complete encapsulation of the SnO_2 nanoparticles.

The SnO_2–C electrodes were electrochemically cycled between 0.005 and 2 V in Li half cells. The first two cycles were an activation process, in which a solid electrolyte interface (SEI) forms with an irreversible capacity loss.[47] The third and following charge–discharge cycles at 0.5 A g^{-1} are presented in Fig. 4. SnO_2(57)–C exhibits a high specific capacity of 630 mA h g^{-1} after 50 cycles, suggesting the cycle stability of this sample even at a high rate of 0.5 A g^{-1}. SnO_2(40)–C and SnO_2(75)–C both deliver a relatively low specific capacity of 470 mA h g^{-1}. The specific capacity of the SnO_2–C hybrids at a high current density is related to both the SnO_2 content and the charge/ion transfer speed. A high SnO_2 content may provide more active material but block the transfer pathway of lithium ions. Thus, it is important to control the SnO_2 loading ratio to obtain a high performance of the LIC. The SnO_2–C hybrid with a 57 wt% SnO_2 content offers an easy accessible diffusion path in the nanocrystalline SnO_2, which possesses a large amount of mesoporosity fully proved by nitrogen sorption measurements. Moreover, the high stable capacities and excellent rate capabilities of the SnO_2–C electrodes are superior for the LIC anode.

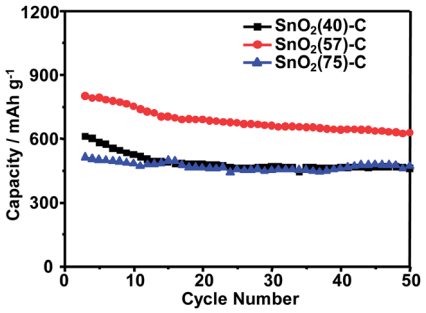

Fig. 4 The charge–discharge cycling performance of SnO_2(40)–C, SnO_2(57)–C, and SnO_2(75)–C at a current density of 0.5 A g^{-1}.

3.3 Electrochemical performance of the lithium ion capacitor

Subsequently, we placed the LIC in a $LiPF_6$-containing organic electrolyte. The overall process for the lithium ion capacitor is not a "rocking-chair" type reaction, as in LIBs, but a cation and anion consuming reaction. On the SnO_2–C electrode, lithium ion intercalation–deintercalation occurs in the charge–discharge process. On the TMC electrode, PF_6^- undergoes an adsorption–desorption process akin to what occurs in EDLCs.

Since the operating potential range between the SnO_2–C and TMC electrodes in the organic electrolyte is three times that in the aqueous electrolyte, the specific energy and power are considerably higher in the former which means a better Ragone performance. The operation potential was tested in the range of 0.005–4.5 V *vs.* Li/Li^+ according to the decomposition voltage of the organic electrolyte for LIBs which is over 4.5 V *vs.* Li/Li^+.[48,49] As seen in the cyclic voltammetry curves (Fig. S3†), polarization is obviously observed near 4.5 V. Furthermore, the potential range was limited to a low value of 0.5 V to avoid the reduction of Li^+ and subsequent plating of the lithium metal at 0–0.5 V *vs.* Li/Li^+. The formation of Li dendrites or mossy lithium from reduced Li^+ may shorten the cell lifetime and lead to a significant safety problem. Therefore, it seems necessary to limit the potential window for the CV experiment to 0.5–4 V *vs.* Li/Li^+.

Interfacial reactions including lithium ion intercalation/deintercalation, electrolyte decomposition, and the formation of a solid electrolyte interphase (SEI) layer determine the irreversible capacity loss and the cycle life of LIB systems.[4,50] The large irreversible capacity observed in the first charge–discharge cycle is a common phenomenon for carbon and metal oxide materials due to the formation of SEI films on the electrode surface.[51,52] To solve the above-mentioned issues through the extended potential swing of the cathode, pre-lithiation is a feasible approach by enabling an increase in the initial efficiency and the suppression of the irreversible capacity of the anode.[53,54] Prior to full LIC cell assembly, the SnO_2–C electrode was pre-lithiated by a simple surface treatment, specifically by placing the electrolyte-wetted SnO_2–C electrodes in direct contact with the Li metal for about 60 min.[55] By this method, the initial coulombic efficiency of the LIC can be improved to 84% from 10% (see Fig. S4†).

LIC full cells with TMC as a cathode and the SnO_2–C hybrid as an anode were developed as samples C//SnO_2(X)–C (X = content of SnO_2), namely C//SnO_2(40)–C, C//SnO_2(57)–C, and C//SnO_2(75)–C. The measured CV curves of C//SnO_2–C in a 1 M $LiPF_6$ LIB electrolyte are shown in Fig. 5a. The shapes, especially at a low scan rate, are approximately rectangular, indicating that the anode and cathode were well matched. The rectangular shape of C//SnO_2(57)–C is noticeable even at a high scan rate as shown in Fig. 5b, and this is believed to be due to fast charge/ion transfer in the anode.

Charge–discharge tests (Fig. 5c) were used to calculate the gravimetric capacitance. They are triangular in shape and exhibit small ohmic drops related to the resistivity of C//SnO_2–C. The capacitance retention ratios are evaluated (Fig. 5d). The capacitances of C//SnO_2(40)–C, C//SnO_2(57)–C and C//SnO_2(75)–C are

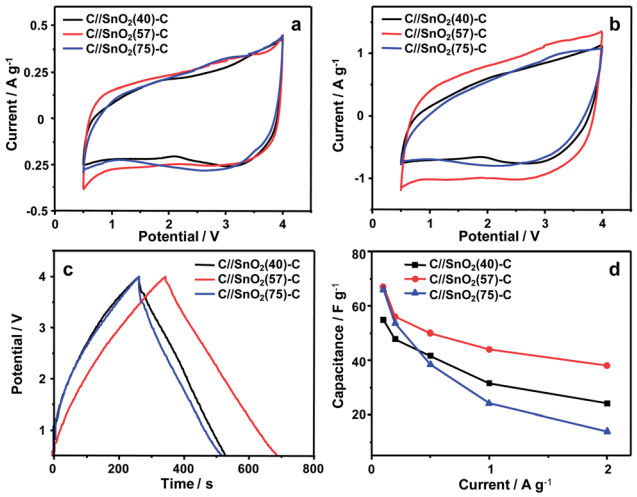

Fig. 5 CV curves of C//SnO_2–C at a scan rate of (a) 5 mV s^{-1} and (b) 20 mV s^{-1}, (c) galvanostatic charge–discharge curves of C//SnO_2–C at 0.3 A g^{-1}, and (d) capacitance retention of C//SnO_2–C with increasing current density.

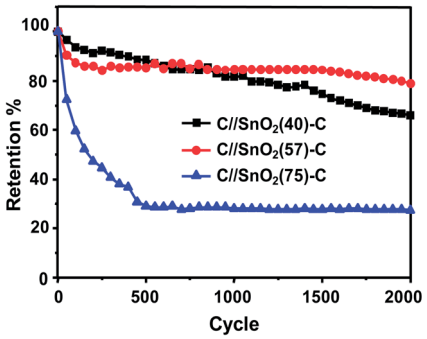

Fig. 6 The long-term cycling performance of C//SnO_2–C at a current density of 1 A g^{-1}.

55, 67 and 66 F g^{-1} at 0.1 A g^{-1}, respectively. It is noticed that both C//SnO_2(57)–C and C//SnO_2(75)–C achieve a higher capacitance than does C//SnO_2(40)–C because a high loading ratio results in more SnO_2 reacting in the charge–discharge process. In a fast charge–discharge process at 0.5 A g^{-1}, the capacitance of C//SnO_2(57)–C (50 F g^{-1}) is higher than those of both C//SnO_2(40)–C (42 F g^{-1}) and C//SnO_2(75)–C (38 F g^{-1}). Obviously, the variation tendency of these capacitances in the full cell is the same as those of SnO_2–C's capacitances in a single electrode. Moreover, the capacitance of C//SnO_2(57)–C remains at 40 F g^{-1} at 2 A g^{-1}. The best SnO_2–-loaded sample, C//SnO_2(57)–C, displays not only a larger capacitance for a small current density, but also a better rate capability in the high rate charge–discharge process, benefiting from the high active material content and the incompletely packed tubular channels for ionic diffusion. Therefore, one should balance the active material content and the ionic diffusion speed through controlling the SnO_2 loading, especially for a long-life time capacitor that allows fast charge–discharge cycles.

Fig. 6 shows the cycling performance of C//SnO_2–C after long-term cycling at a current density of 1 A g^{-1}. As might be expected, the capacitance retention of C//SnO_2(57)–C is higher than that of both C//SnO_2(40)–C and C//SnO_2(75)–C and still retains 80% of its initial value after 2000 cycles. Besides having the best active material content and high ionic diffusion speed, the high capacitance retention of C//SnO_2(57)–C also reveals that such a unique carbon host prevents the agglomeration of SnO_2 nanoparticles and stabilizes the long-term cycling performance.

In the first five hundred cycles, the capacitance retention of C//SnO_2(40)–C with the lowest SnO_2 content is higher than that of C//SnO_2(57)–C and C//SnO_2(75)–C due to its faster ionic diffusion. In order to support the fast adsorption–desorption of PF_6^- on the cathode, the anode in the full cell demands a higher ionic diffusion rate than that in a three-electrode system.[7] Consequently, the capacitance retention of the LIC is quite different from that of a SnO_2–C hybrid anode in a three-electrode system. However, after thousands of cycles the unfilled channel may result in agglomeration of SnO_2 nanoparticles. Meanwhile, the high SnO_2 loading might lead to a blockage in the channels of the TMC matrix. It is obvious that a correct SnO_2 content is needed to retain the original nano-structure of the hybrid and furthermore results in a superior high rate capacity over a large number of cycles.

To further probe the origin of the capacitance fade, EIS was performed on C//SnO_2–C at an OCV of 2.6 V. These spectra were recorded in the range from 10 mHz to 0.1 MHz with a signal amplitude of 5 mV. All parameters related to mass and charge transport reflect the superposition of both electrodes for the impedance of the complex system. The results represent a total contribution from both anode and cathode. Nyquist plots of lithium ion capacitors before and after 2000 charge–discharge cycles are shown in Fig. 7a and b, respectively. EIS was also fitted by an electric equivalent circuit model as shown in Fig. 7c.

It is noted that there are no overlapping depressed semicircles associated with the migration of lithium ions through SEI layers, different from previous studies.[56,57] The exact reasons behind this difference are not fully understood, but one possible reason may be that circles associated with the migration of lithium ions exactly superimpose on the later semicircle associated with intercalation type reactions and characterized by a charge transfer resistance R_{CT} in the high to medium frequency region. The phenomenon may indicate that the SEI layer resistance of SnO_2–C is so low that the relevant semicircle is entirely covered by that of R_{CT}. Meanwhile, the "disappearing SEI layer resistance" reflects the fast lithium ion migration in SnO_2–C, corresponding to the Nyquist plot of the SnO_2–C half-cell (Fig. S5†).

The fitting resistances of each component in C//SnO_2–C are listed in Table 2. All values due to the ohmic resistance (R_S), charge transfer resistance (R_{CT}), and the Warburg element (R_W) are presented before and after long-term cycles. It is reasonable that the Li-ion conductivity and diffusivity in both liquid and solid phases decrease with long-term continuous charge–discharge. The resistance R_S at the interception with the real axis can be ascribed to the electrolyte, separator and contacts, and correlates with the ohmic polarization of the capacitor.[58] As

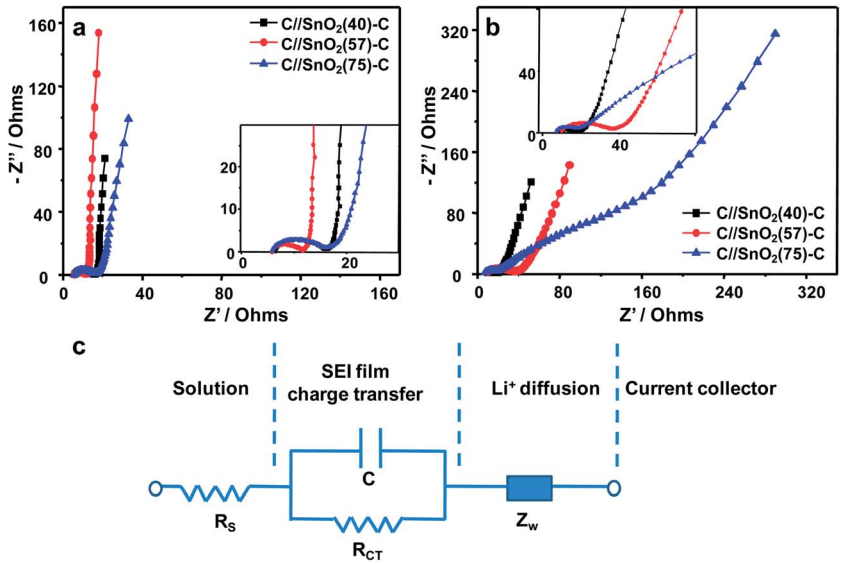

Fig. 7 The Nyquist plots of C//SnO_2–C (a) before and (b) after 2000 charge–discharge cycles, and (c) electric equivalent circuit model of C//SnO_2–C.

Table 2 The fitting resistance of each component and the diffusion coefficient of C//SnO_2–C

	R_S/Ohm	R_{CT}/Ohm	R_W/Ohm	W_T/s	D_{Li^+}/nm^2 s^{-1}
Uncycled samples					
C//SnO_2(40)–C	5.9	9.7	5.4	1.0	4
C//SnO_2(57)–C	5.8	5.4	4.0	0.35	1.9
C//SnO_2(75)–C	5.6	9.8	10.8	1.3	11.4
Samples after 2000 cycles					
C//SnO_2(40)–C	4.4	7.2	24.6	2.07	3.0
C//SnO_2(57)–C	8.1	30.9	22.0	1.3	3.1
C//SnO_2(75)–C	9.8	9.1	281.4	20.6	0.2

seen in Fig. 7a, before cycling, the R_S of all samples is in the range of 5.6–5.9 Ohms. R_W mainly represents the Li-ion diffusion rate in a device. The R_W values of C//SnO_2(40)–C and C//SnO_2(57)–C are 5.4 and 4.0 Ohms, respectively, which are lower than that of C//SnO_2(75)–C (10.8 Ohms), suggesting that these two C//SnO_2–C materials have faster Li-ion diffusion than C//SnO_2(75)–C. In general, the surfaces of an electrode can be modified by the formation of the SEI membrane during the charge–discharge process. Thus, the R_W value increases after 2000 cycles, as listed in Table 2. In addition, the vertical line in the low frequency region reflects the capacitive behavior of TMC and the SnO_2–C hybrid.

The Nyquist plots after 2000 charge–discharge cycles are collected in Fig. 7b. The Warburg slope lines depart from the initial location in varying amounts. The deviation of the Warburg lines reflects the structure stability of SnO_2–C, which plays an important role in the improvement of the capacitance retention. Specifically, the R_W values of C//SnO_2(40)–C and C//SnO_2(57)–C are fitted as 24.6 and 22.0 Ohms respectively, while that of C//SnO_2(75)–C unfortunately increases to 281.4 Ohms. The retention of the R_W value of C//SnO_2(40)–C and C//SnO_2(57)–C confirms the stability of the SnO_2–C hybrid. Their capacity retentions are almost identical and much higher than that of C//SnO_2(75)–C.

Besides R_W, the diffusion coefficient of Li^+ (D_{Li^+}) can further confirm this explanation. The lithium ion flux in the solid intercalation compound electrode of a conventional lithium-ion battery may be reasonably described by Fick's first law of diffusion.[59] D_{Li^+} of the LIC was calculated using the following formula:[16]

$$D_{Li^+} = \frac{L^2}{W_T} \quad (5)$$

where L is the average diffusion distance, that is the radius of the SnO_2 nanoparticles (~2 nm) observed in the TEM image, and W_T is the Warburg diffusion element listed in Table 2. As seen in Table 2, the diffusion coefficients of the uncycled samples and samples after 2000 cycles are listed. It can be envisaged that the higher SnO_2 loading indicates the larger accessible surfaces of SnO_2 nanoparticles considering the electrodes with an identical weight. This might be the reason that before cycling, the diffusion coefficient of SnO_2(75)–C with the highest SnO_2 loading is higher than that of the samples with lower SnO_2 loadings. While, after 2000 cycles, the volume expansion and pulverization of SnO_2 in sample SnO_2(75)–C would cause the loose contact between the particles, thus lowering the diffusion coefficient.

The calculated D_{Li^+} of both C//SnO_2(40)–C and C//SnO_2(57)–C remains constant at 3 nm^2 s^{-1}, while that of C//SnO_2(75)–C decreases from 11.4 nm^2 s^{-1} to 0.2 nm^2 s^{-1}. These data clearly demonstrate that the SnO_2(40)–C and SnO_2(57)–C hybrids maintain open and fast ionic diffusion after thousands of cycles. The LIC with the best SnO_2 loading ratio (57 wt%) has a high capacitance and cycle stability derived from the higher loading ratio and better integrity of the SnO_2–C hybrid. The capacity of the anode commonly increases with increasing SnO_2

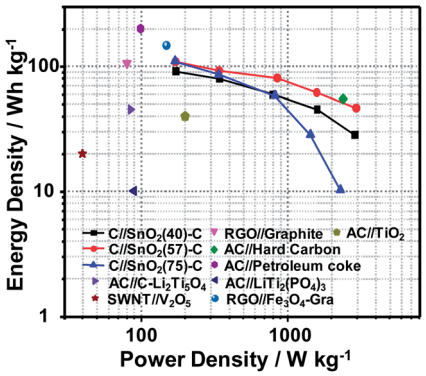

Fig. 8 The Ragone plots of C//SnO_2–C. Values reported for other lithium ion capacitors are added for comparison.[10,34,60–64]

loading, as well as the capacitance of the whole LIC. Meanwhile the elastic amorphous carbon can buffer SnO_2 nanoparticles from expansion during the charge–discharge process, which will improve the cycle life.

Energy density and power density have been widely used to evaluate the performance of electrochemical devices. Fig. 8 compares the power and energy densities of C//SnO_2–C reported in this work to the values reported for non-aqueous lithium ion capacitors. All data were based on the mass of the active material on both anode and cathode sides. The Ragone plots show that C//SnO_2(57)–C has a maximum energy density of 110 W h kg^{-1} and can achieve a maximum power density of 2960 W kg^{-1}. The energy density of C//SnO_2(57)–C is considerably higher than those of C//SnO_2(40)–C and C//SnO_2(75)–C. For instance, C//SnO_2(57)–C can achieve a remarkable energy density of 62 W h kg^{-1} at a current density of 1 A g^{-1}, which is over twice that of the C//SnO_2(75)–C capacitor (28 W h kg^{-1}). Significantly, the energy densities of C//SnO_2–C are also substantially higher than or at least comparable to those of recently reported non-aqueous lithium ion capacitors.[10,34,60–64] For an assembled supercapacitor device (comprising a current collector, active material, binder and separator), the specific volumetric energy was calculated to be 124–152 mW h cm^{-3} for the three kinds of SnO_2–C hybrid based LICs. The value is two orders of magnitude higher than that (<1 mW h cm^{-3}) of the typical activated carbon supercapacitors.[65,66] Apart from that, the energy density of the lithium ion capacitor is comparable to that of lithium ion batteries, and the power density also approaches that of symmetric supercapacitors, which makes it possible to bridge the performance gap between LIBs and supercapacitors.

4. Summary

We investigated the electrochemical performance of several porous carbons (TMC, HPC and YP47) as the cathode of LICs. The results reveal that tubular mesoporous carbon with a high surface area and pore volume exhibits the largest capacitance and good rate capability. Based on the tubular mesoporous carbon as a cathode and a SnO_2–C hybrid as an anode, a new non-aqueous LIC was fabricated. The capacitance of the whole LIC increases with increasing SnO_2 loading ratio in the anode. By investigating LICs with different SnO_2 contents in the anode, it has been shown that the LIC with a moderate SnO_2 content (57%) in the anode matrix gives the highest energy density (110 W h kg^{-1}) and capacitance retention (80% at 2000 cycles). The outstanding performance of the LIC is substantially related to the structure of the SnO_2–C hybrid. The TMC matrix in SnO_2–C provides channels for ionic diffusion in the center of the tubes and highly conductive surrounding material for electron transport. It also prevents the SnO_2 nanoparticles from agglomeration. However, an excessive loading ratio may cause a blockage in the channels of the TMC matrix. Only the optimum loading ratio can both keep the SnO_2 nanoparticles stable in long-term cycles and the fast charge–discharge process by offering an adequate pathway for ionic diffusion. More work is needed to clearly understand the ionic diffusion between the anode and cathode materials.

Acknowledgements

This project was supported by the National Natural Science Foundation of China (no. 21376047) and the Fundamental Research Funds for the Central Universities (DUT12ZD218).

References

1 N.-S. Choi, Z. Chen, S. A. Freunberger, X. Ji, Y.-K. Sun, K. Amine, G. Yushin, L. F. Nazar, J. Cho and P. G. Bruce, *Angew. Chem., Int. Ed.*, 2012, **51**, 9994–10024.
2 *Electrochemical Supercapacitors: Scientific Fundamentals and Technological Applications*, ed. B. E. Conway, 1999.
3 B. Dunn, H. Kamath and J. M. Tarascon, *Science*, 2011, **334**, 928–935.
4 V. Etacheri, R. Marom, R. Elazari, G. Salitra and D. Aurbach, *Energy Environ. Sci.*, 2011, **4**, 3243.
5 K. Naoi, S. Ishimoto, J.-i. Miyamoto and W. Naoi, *Energy Environ. Sci.*, 2012, **5**, 9363.
6 D. Cericola and R. Kötz, *Electrochim. Acta*, 2012, **72**, 1–17.
7 A. Du Pasquier, I. Plitz, S. Menocal and G. Amatucci, *J. Power Sources*, 2003, **115**, 171–178.
8 G. G. Amatucci, F. Badway, A. Du Pasquier and T. Zheng, *J. Electrochem. Soc.*, 2001, **148**, A930–A939.
9 T. Aida, K. Yamada and M. Morita, *Electrochem. Solid-State Lett.*, 2006, **9**, A534–A536.
10 H.-G. Jung, N. Venugopal, B. Scrosati and Y.-K. Sun, *J. Power Sources*, 2013, **221**, 266–271.
11 V. Khomenko, E. Raymundo-Piñero and F. Béguin, *J. Power Sources*, 2008, **177**, 643–651.
12 K. Naoi, S. Ishimoto, Y. Isobe and S. Aoyagi, *J. Power Sources*, 2010, **195**, 6250–6254.
13 J. Ni, Y. Huang and L. Gao, *J. Power Sources*, 2013, **223**, 306–311.
14 W. H. Shin, H. M. Jeong, B. G. Kim, J. K. Kang and J. W. Choi, *Nano Lett.*, 2012, **12**, 2283–2288.

15 M. D. Stoller, S. Murali, N. Quarles, Y. Zhu, J. R. Potts, X. Zhu, H.-W. Ha and R. S. Ruoff, *Phys. Chem. Chem. Phys.*, 2012, **14**, 3388–3391.
16 B. Z. Jang, C. Liu, D. Neff, Z. Yu, M. C. Wang, W. Xiong and A. Zhamu, *Nano Lett.*, 2011, **11**, 3785–3791.
17 Y.-Q. Wang, L. Gu, Y.-G. Guo, H. Li, X.-Q. He, S. Tsukimoto, Y. Ikuhara and L.-J. Wan, *J. Am. Chem. Soc.*, 2012, **134**, 7874–7879.
18 B. Li, C. Han, Y.-B. He, C. Yang, H. Du, Q.-H. Yang and F. Kang, *Energy Environ. Sci.*, 2012, **5**, 9595–9602.
19 L. Zhao, Y.-S. Hu, H. Li, Z. Wang and L. Chen, *Adv. Mater.*, 2011, **23**, 1385–1388.
20 S. S. Zhang, K. Xu and T. R. Jow, *J. Power Sources*, 2006, **160**, 1349–1354.
21 J. Wang, N. Yang, H. Tang, Z. Dong, Q. Jin, M. Yang, D. Kisailus, H. Zhao, Z. Tang and D. Wang, *Angew. Chem.*, 2013, **52**, 6417–6420.
22 J. S. Chen and X. W. Lou, *Small*, 2013, **9**, 1877–1893.
23 Z. Wang, D. Luan, S. Madhavi, Y. Hu and X. W. Lou, *Energy Environ. Sci.*, 2012, **5**, 5252–5256.
24 S. Ding, Z. Wang, S. Madhavi and X. W. Lou, *J. Mater. Chem.*, 2011, **21**, 13860–13864.
25 X. Lai, J. E. Halpert and D. Wang, *Energy Environ. Sci.*, 2012, **5**, 5604–5618.
26 Z. Dong, H. Ren, C. M. Hessel, J. Wang, R. Yu, Q. Jin, M. Yang, Z. Hu, Y. Chen, Z. Tang, H. Zhao and D. Wang, *Adv. Mater.*, 2013, **26**, 905–909.
27 J. Jiang, Y. Li, J. Liu, X. Huang, C. Yuan and X. W. D. Lou, *Adv. Mater.*, 2012, **24**, 5166–5180.
28 C. Lei, F. Han, D. Li, W.-C. Li, Q. Sun, X.-Q. Zhang and A.-H. Lu, *Nanoscale*, 2013, **5**, 1168–1175.
29 Z. Wang, J. S. Chen, T. Zhu, S. Madhavi and X. W. Lou, *Chem. Commun.*, 2010, **46**, 6906–6908.
30 S. Yang, X. Feng, S. Ivanovici and K. Müllen, *Angew. Chem., Int. Ed.*, 2010, **49**, 8408–8411.
31 F. Han, W.-C. Li, M.-R. Li and A.-H. Lu, *J. Mater. Chem.*, 2012, **22**, 9645–9651.
32 V. Aravindan, N. Shubha, W. C. Ling and S. Madhavi, *J. Mater. Chem. A*, 2013, **1**, 6145–6151.
33 P. Han, W. Ma, S. Pang, Q. Kong, J. Yao, C. Bi and G. Cui, *J. Mater. Chem. A*, 2013, **1**, 5949–5954.
34 F. Zhang, T. Zhang, X. Yang, L. Zhang, K. Leng, Y. Huang and Y. Chen, *Energy Environ. Sci.*, 2013, **6**, 1623–1632.
35 A.-H. Lu, W.-C. Li, W. Schmidt, W. Kiefer and F. Schüth, *Carbon*, 2004, **42**, 2939–2948.
36 A.-H. Lu, W. Schmidt, B. Spliethoff and F. Schüth, *Chem.–Eur. J.*, 2004, **10**, 6085–6092.
37 A. H. Lu, W. Schmidt, B. Spliethoff and F. Schuth, *Adv. Mater.*, 2003, **15**, 1602–1606.
38 G.-P. Hao, W.-C. Li, D. Qian, G.-H. Wang, W.-P. Zhang, T. Zhang, A.-Q. Wang, F. Schüth, H.-J. Bongard and A.-H. Lu, *J. Am. Chem. Soc.*, 2011, **133**, 11378–11388.
39 L. L. Zhang and X. S. Zhao, *Chem. Soc. Rev.*, 2009, **38**, 2520.
40 A. Ghosh and Y. H. Lee, *ChemSusChem*, 2012, **5**, 480–499.
41 Z. Weng, F. Li, D.-W. Wang, L. Wen and H.-M. Cheng, *Angew. Chem., Int. Ed.*, 2013, **52**, 3722–3725.
42 Z. Li, N. Liu, X. Wang, C. Wang, Y. Qi and L. Yin, *J. Mater. Chem.*, 2012, **22**, 16640–16648.
43 L. Shen, X. Zhang, E. Uchaker, C. Yuan and G. Cao, *Adv. Energy Mater.*, 2012, **2**, 691–698.
44 I. C. f. D. Data, in Powder Diffraction File.
45 Y. Qin, J. Lu, P. Du, Z. Chen, Y. Ren, T. Wu, J. T. Miller, J. Wen, D. J. Miller, Z. Zhang and K. Amine, *Energy Environ. Sci.*, 2013, **6**, 519.
46 E. Fabbri, L. Bi, D. Pergolesi and E. Traversa, *Energy Environ. Sci.*, 2011, **4**, 4984.
47 I. T. Lucas, E. Pollak and R. Kostecki, *Electrochem. Commun.*, 2009, **11**, 2157–2160.
48 R. Herr, *Electrochim. Acta*, 1990, **35**, 1257–1265.
49 A. Kraytsberg and Y. Ein-Eli, *Adv. Energy Mater.*, 2012, **2**, 922–939.
50 R. Marom, S. F. Amalraj, N. Leifer, D. Jacob and D. Aurbach, *J. Mater. Chem.*, 2011, **21**, 9938–9954.
51 F. Han, D. Li, W.-C. Li, C. Lei, Q. Sun and A.-H. Lu, *Adv. Funct. Mater.*, 2013, **23**, 1692–1700.
52 N. A. Kaskhedikar and J. Maier, *Adv. Mater.*, 2009, **21**, 2664–2680.
53 Z. L. Wang, D. Xu, H. G. Wang, Z. Wu and X. B. Zhang, *ACS Nano*, 2013, **7**, 2422–2430.
54 S. R. Sivakkumar and A. G. Pandolfo, *Electrochim. Acta*, 2012, **65**, 280–287.
55 J.-S. Bridel, S. Grugeon, S. Laruelle, J. Hassoun, P. Reale, B. Scrosati and J.-M. Tarascon, *J. Power Sources*, 2010, **195**, 2036–2043.
56 W. J. Cao and J. P. Zheng, *J. Power Sources*, 2012, **213**, 180–185.
57 M. D. Levi, G. Salitra, B. Markovsky, H. Teller, D. Aurbach, U. Heider and L. Heider, *J. Electrochem. Soc.*, 1999, **146**, 1279–1289.
58 P. L. Moss, G. Au, E. J. Plichta and J. P. Zheng, *J. Power Sources*, 2009, **189**, 66–71.
59 *Environmental Hydrology*, ed. V. P. Singh, 1995.
60 V. Aravindan, W. Chuiling, M. V. Reddy, G. V. S. Rao, B. V. R. Chowdari and S. Madhavi, *Phys. Chem. Chem. Phys.*, 2012, **14**, 5808–5814.
61 V. Aravindan, Y. L. Cheah, W. F. Mak, G. Wee, B. V. R. Chowdari and S. Madhavi, *ChemPlusChem*, 2012, **77**, 570–575.
62 J.-H. Kim, J.-S. Kim, Y.-G. Lim, J.-G. Lee and Y.-J. Kim, *J. Power Sources*, 2011, **196**, 10490–10495.
63 D.-W. Wang, H.-T. Fang, F. Li, Z.-G. Chen, Q.-S. Zhong, G. Q. Lu and H.-M. Cheng, *Adv. Funct. Mater.*, 2008, **18**, 3787–3793.
64 M. Schroeder, M. Winter, S. Passerini and A. Balducci, *J. Power Sources*, 2013, **238**, 388–394.
65 G.-P. Hao, A.-H. Lu, W. Dong, Z.-Y. Jin, X.-Q. Zhang, J.-T. Zhang and W.-C. Li, *Adv. Energy Mater.*, 2013, **3**, 1421–1427.
66 Y. Gogotsi and P. Simon, *Science*, 2011, **334**, 917–918.